



Contents lists available at ScienceDirect

Engineering Science and Technology, an International Journal

journal homepage: www.elsevier.com/locate/jestch

A compact complementary split ring resonator (CSRR) based perfect metamaterial absorber for energy harvesting applications



Najeeb Ullah ^{a,b}, Md. Shabiul Islam ^{a,*}, Ahasanul Hoque ^{c,*}, Wong Hin Yong ^a, Mohamed S. Soliman ^{d,e}, Saleh Albadran ^f, Mohammad Tariqul Islam ^{g,*}

^a Faculty of Engineering (F.O.E.), Multimedia University (MMU), 63100 Cyberjaya, Selangor, Malaysia

^b Faculty of I.C.T., BUITEMS, 87300 Quetta, Balochistan, Pakistan

^c Institute of Climate Change, Universiti Kebangsaan Malaysia, Bangi 43600, Malaysia

^d Department of Electrical Engineering, College of Engineering, Taif University, P.O. Box 11099, Taif 21944, Saudi Arabia

^e Department of Electrical Engineering, Faculty of Energy Engineering, Aswan University, Aswan 81528, Egypt

^f Department of Electrical Engineering, College of Engineering, University of Hail, Hail 55211, Saudi Arabia

^g Department of Electrical, Electronic and Systems Engineering, Faculty of Engineering and Built Environment, Malaysia

ARTICLE INFO

Article history:

Received 26 March 2023

Revised 30 May 2023

Accepted 26 June 2023

Available online 12 July 2023

Keywords:

Metamaterial

Perfect metamaterial absorber

Energy harvesting

ABSTRACT

A novel Compact Complementary Split Ring Resonator (CSRR) metamaterial unit cell with perfect absorption, beneficial for ambient power harvesting, is proposed to operate in the S- and C-band. The size of the structure is $15 \times 15 \times 1.575 \text{ mm}^3$ with dimensions of $0.18\lambda_0 \times 0.18\lambda_0 \times 0.019\lambda_0$ at the lowest absorption frequency. The proposed compact-sized CSRR structure exhibits notable characteristics such as high absorption coefficients and polarization-insensitive behaviours across a wide range of angles. The results demonstrate a notably high absorption efficiency of 97%, 99%, and 98% at 3.7275 GHz, 4.7075 GHz, and 5.9325 GHz. A 3×3 array is designed and verified by experimental results. The proposed design exhibits superior performance compared to previously published designs, which suffer from significant limitations such as a large metamaterial structure, reduced absorption frequency bands, and a lower fraction of absorption bands. The proposed design exhibits potential for utilization in developing wireless sensor network applications that require compact and highly efficient harvesting systems.

© 2023 Karabuk University. Publishing services by Elsevier B.V. This is an open access article under the CC BY-NC-ND license (<http://creativecommons.org/licenses/by-nc-nd/4.0/>).

1. Introduction

The growth of new technologies like 5G networks and the Internet of Things (IoT) has led to a significant increase in wireless sensor networks (W.S.N.s) [1–3]. Consequently, the sensor nodes are deployed both statically and dynamically. A typical wireless node uses battery power but has a limited life cycle. When the energy of the source node is diminished, it cannot fulfill its role in the sensor network unless it is restored or some energy harvesting techniques are introduced to meet the requirement. In addition, many challenges are linked with batteries, such as current leakages (using a battery, even if not in use), the effect of severe weather conditions (may break down the batteries), and chemical leakage (may cause several environmental problems).

Moreover, sensor nodes demand an uninterrupted power supply [4]. Therefore, the energy harvesting system has become essential in obtaining energy from the environment and supplying this energy to sensing nodes, batteries, and low-energy electronic devices. The necessity to lower the power consumption of W.S.N.s and improve the power provided by energy harvesters has prompted substantial research on battery-powered wireless sensor nodes (W.S.N.s). In recent studies, energy harvesting techniques for thermal, wind, solar, and electromagnetic energy (EM) have been proposed [5]. Moreover, EM harvesting techniques have attracted much attention because of their omnipresence in the environment [6].

Furthermore, EM collector design plays a vital role in capturing and transferring the energy used by wireless sensor nodes [7,8]. Some other design structures, such as metamaterial absorbers, antenna arrays and rectennas, have been proposed [9,10]. Metamaterials are materials whose electromagnetic characteristics are derived from their structure rather than their chemical composition.

* Corresponding authors.

E-mail addresses: 1221400623@student.mmu.edu.my, najeeb.ullah1@buitms.edu.pk (N. Ullah), shabiul.islam@mmu.edu.my (M.S. Islam), ahasanul@ukm.edu.my (A. Hoque), hywong@mmu.edu.my (W.H. Yong), soliman@tu.edu.sa (M.S. Soliman), s.abadran@uoh.edu.sa (S. Albadran), tariqul@ukm.edu.my (M.T. Islam).

On the other hand, metamaterial absorbers are regularly spaced unit cells on a two-dimensional plane with unique features such as negative permittivity and magnetic permeability [11]. Metamaterial absorbers have many applications in antenna miniaturization [12,13], sensors [14], and many more [15]. Metamaterial absorbing structures exhibit strong resonances and pure surface resistivity. Additionally, the metamaterial absorber's size is substantially less than that of the traditional system, i.e. metamaterial absorber is much smaller than the conventional system based on antennas, which makes it more efficient in electromagnetic energy harvesting systems [5]. The metamaterial's structural design is associated with capacitance and inductance, receives EM waves at resonant frequencies, and stores energy in electrical and magnetic forms [5,16]. The received energy is then dissipated through a load or dielectric substrate. The highest amount of absorption may be obtained if the structural impedance is equal to the open space impedance.

2. Literature review unit cell design structure

In [17], energy harvesting from radio frequency waves was proposed. Their proposed metamaterial structure receives R.F. waves from the GSM band, which are converted to D.C. voltage by Schotky diodes. A metamaterial multiband antenna consisting bidirectional complementary split-ring resonator (CSRR) and four rectifiers has been proposed in [18]. The CSRR structure was designed on an FR-4 substrate, which operates at four resonant frequencies 1.8 GHz (GSM), 2.1 GHz (UMTS), 2.45 GHz (WiFi), and 2.6 GHz (4G) (GSM). In [19], Almutairi et al. presented a complementary split-ring resonator (CSRR)-based metamaterial for C band applications. The design was printed on an FR-4 substrate, and three-square split ring resonators (SSRR) are interconnected with strip lines to enhance the coupling effect. In [20], Sankar et al. proposed a circular complementary split resonator for R.F. energy harvesting in the I.S.M. band. The presented design operates at a 2.4 GHz resonant frequency. In [21], a complementary split-ring resonator with a backdrop plane was presented. The authors claim that the designed structural model is low profile and efficient for a wide range of radiance angles placed on metallic surfaces. Their proposed structural design operates at a resonant frequency of 5.8 GHz. In [22], a Ground-backed Complementary Split-Ring Resonator (G-CSRR) array was presented. The authors conducted a comparative survey of power harvesting efficiency in the proposed study using numerical analysis and laboratory measurements. A microstrip patch antenna array and G-CSRR were compared and studied. The authors claim that 92% of power conversion efficiency is achieved with G-CSRR. In [23], a wideband Ground-backed Complementary Split-Ring Resonator (WG-CSRR) array was presented. Numerical analysis was used to perform a comparison study between power harvesting efficiency and frequency bandwidth. The authors also compared the W.G.- CSRR array, G- CSRR array and microstrip patch antenna array. According to the author, W.G.- CSRR achieves substantially higher bandwidth than G- CSRR. In [24], Das et al. proposed an energy-harvesting metamaterial based on the Complementary Split Ring Resonator (CSRR) and a polydimethylsiloxane (PDMS) substrate. The backed-ground plane is employed to enhance absorption in the proposed study, and via load is used to boost power harvesting efficiency. The authors also claim their design suits unity efficiency and high-quality factor (Q-factor). A review paper on R.F. energy harvesting based on different metamaterials and metasurfaces is presented in [5]. The proposed article discusses E.H. and summarizes several theoretical and experimental analyses on metasurface/metamaterial-based E.H. systems. For visible spectrum solar energy scavenging, a tri-layer metallic optical thin film

broadband nanostructure metamaterial absorber is presented in [25]. The authors propose a metamaterial absorber utilizing lumped elements in reference [26]. The design exhibits dual resonance behaviour, manifesting at frequencies of 3.8 GHz and 6.8 GHz and achieving a degree of absorption exceeding 90%. A broadband ultra-thin absorber for air defence applications was presented in [27]. Theoretically, an FWHM bandwidth of 0.42 GHz with a percentage of 8.13 has been observed within the frequency range of 4.94–5.36 GHz. The authors propose a metamaterial absorber that utilizes CRRs with lumped elements for the purpose of microwave energy harvesting, as described in [28]. The article referenced as [29] introduced a dual-layer metamaterial absorber in the shape of an 8-point star ring. The absorber was found to exhibit absorption rates of 98.96%, 98.7%, and 99.43% at frequencies of 1.8 GHz, 2.14 GHz, and 2.57 GHz, respectively. The authors proposed a dual-band metamaterial absorber in reference [30], which is comprised of a closed ring resonator and operates at frequencies of 2.09 GHz and 2.54 GHz. In [31], a microwave metamaterial absorber that is ultrathin, wide-angle, and exhibits polarization independence was presented. Absorbance values of 99.37% and 97.18% were obtained at frequencies of 2.13 GHz and 2.52 GHz, respectively.

Various studies have been proposed in this field of metamaterial-based energy harvesting. Yet, their designs have several drawbacks, such as a huge metamaterial structure, fewer absorption frequency bands, and some with a lower proportion of absorption bands. This paper offers a new compact-size Complementary Split Ring Resonator (CSRR) metamaterial with three resonant frequencies: 3.7275 GHz, 4.7075 GHz, and 5.9325 GHz. In these bands, the proposed structure has negative permittivity and permeability. The proposed structure has 97%, 99%, and 98% absorption efficiencies. Compared with other designed structures, the proposed structure has some significant improvements. The unit cell first resonated at three distinct frequencies. Second, absorption is very close to unity at all resonant frequencies.

3. Unit cell design structure

Fig. 1 (a) shows the top view CSRR unit cell generated in C.S.T. for the suggested design. The Finite Difference Time Domain (FDTD) approach is used by C.S.T. [32]. The unit cell is developed and produced with a 1.575 mm thick Rogers RT 5880 substrate dielectric material. The permittivity (ϵ) and loss tangent (δ) are 2.2 and 0.0009, respectively. Therefore, the overall dimensions of the proposed design and the back-side coated copper are (15 mm × 15 mm), respectively. The proposed design consists of five split ring resonators (SRR) positioned at a 45-degree angle to each other to increase performance. Orienting the SRRs at a 45-degree angle has the potential to improve the coupling mecha-

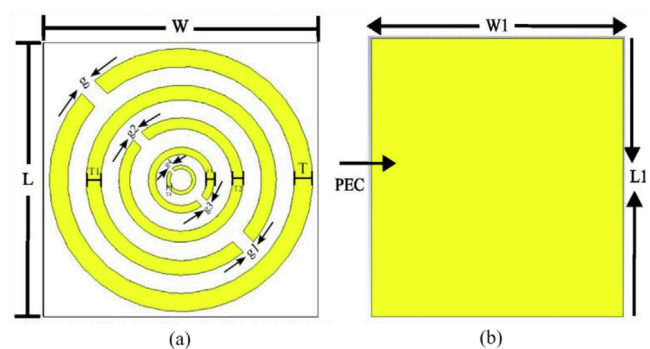


Fig. 1. (a) Top-view of the proposed structure, simulated in CST (b) Back-view of the proposed structure, simulated in CST.

nisms that exist between neighbouring resonators. The diagonal arrangement facilitates the effective interaction between the electric and magnetic field components. The phenomenon can potentially induce a more robust interconnection among adjacent (Split Ring Resonators (SRRs)) yielding superior resonance characteristics and heightened electromagnetic reactivity. These resonators are manufactured of annealed copper. The thickness of the annealed copper is 0.035, where the conductivity ($\sigma = 5.8 \times 10^7 \text{ S/m}$). Therefore, the single resonator's thickness and split gap are the same but different to others. For example, the thickness and split gap of the first resonator is 1 mm, the second resonator is 0.8 mm, the third resonator is 0.6 mm, the fourth resonator is 0.4 mm, and the fifth resonator is 0.2 mm. Therefore, a gap of 1 mm separates the first and second ring resonators, 0.8 mm separates the second and third, 0.6 mm separates the third from the fourth, and 0.4 mm separates the fourth from the fifth ring resonator. The proposed design operates at three resonance frequencies—3.7275 GHz, 4.7075 GHz, and 5.325 GHz—**Fig. 1 (b)** depicts the design back-view. **Fig. 2** illustrates the design's perspective view. **Table 1** summarizes the basic geometrical properties of the unit cell.

4. Methods and techniques

The appropriate boundary conditions were selected when designing the proposed unit cell. We employed perfect magnetic and electric boundary conditions and used Floquet ports. To extract the electromagnetic responses, the proposed design is positioned between two Floquet ports and evacuated by a uniform plan wave propagated along the z-axis under open-end boundary conditions, as illustrated in **Fig. 2**. The unit cell condition, on the other hand, was employed and applied in both the x- and y-coordinates. The unit cell's back side is copper-plated and faces the z-axis. As a result, the electric E and magnetic H fields are polarised along the x and y coordinates, respectively. Tetrahedral meshing methods and frequency domain solvers were employed for the 3 to 6 GHz simulation range.

The reflection coefficient (S_{11}) and transmission coefficient (S_{21}) can be derived from Equations (1) and (2) [33].

$$S_{11} = \frac{R_{01}(1 - e^{i2nk_0d})}{1 - R_{01}^2 e^{i2nk_0d}} \quad (1)$$

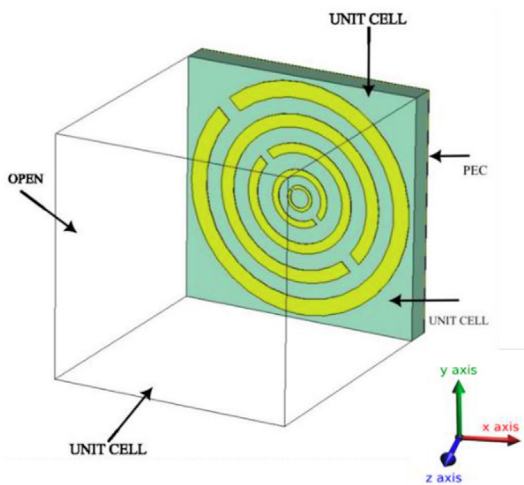


Fig. 2. Boundary condition of the proposed structure during simulation in CST.

Table 1
Descriptions of the structure's dimensions.

Parameters	Dimension (mm)	Parameters	Dimension (mm)
L	15	g	1
W	15	g1	0.8
T	1	g2	0.6
T1	0.8	g3	0.4
T2	0.6	g4	0.2
T3	0.4	W1	15
T4	0.2	L1	15

$$S_{21} = \frac{(1 - R_{01}^2)e^{i2nk_0d}}{1 - R_{01}^2 e^{i2nk_0d}} \quad (2)$$

$$\text{Where } R_{01} = \frac{z-1}{z+1}$$

Furthermore, the metamaterial is classified as a passive medium. In such a scenario, the real and imaginary portion of the refractive index and impedance is determined by the following equations (3) and (4).

$$z(\text{real}) \geq 0 \quad (3)$$

$$n(\text{imaginary}) \geq 0 \quad (4)$$

For the above scenario, the below equation can be used to determine the impedance Z.

$$Z = \pm \sqrt{\frac{(1 + S_{11})^2 - S_{21}^2}{(1 - S_{11})^2 - S_{21}^2}} \quad (5)$$

$$e^{ink_0d} = X \pm i\sqrt{1 - X^2} \quad (6)$$

$$X = 1/2S_{21}(1 - S_{11}^2 + S_{21}^2)$$

The refractive index (n) can be calculated using equation (7), wherein the real component of the equation incorporates a logarithmic function.

$$n = \frac{1}{K_0 d} \{ [\text{[im]aginary}[\ln e^{ink_0d}] + 2m\pi] - i[\text{[re]al}[\ln e^{ink_0d}] \quad (7)$$

Where the variables k_0 , m , and d represent the wave vector in free space, an integer value, and the prototype thickness, respectively.

The relative permeability (μr) and permittivity (ϵ) from the S-parameters were extracted and analyzed using the Nicolson-Ross-Weir (N.R.W.). The N.R.W. is a well-known method for EM characterization. The μr and ϵr can be obtained using the equations below [34].

$$\mu r = \frac{2c(1 - s_{21} + s_{11})}{jwd(1 + S_{21} - S_{11})} \quad (8)$$

$$\epsilon r = \mu r + j \frac{2cS_{11}}{wd} \quad (9)$$

Where c represents the speed of light, ϵr represents relative permittivity, μr represents relative magnetic permeability, and ω represents the angular frequency. S_{11} and S_{21} represent reflected and transmitted power, respectively, where d is the thickness of the slab.

Fig. 3 shows the analysis of the complex scattering parameters S_{11} and S_{21} . The three frequencies at the proposed design resonate at are 3.7275 GHz, 4.7075 GHz, and 5.9325 GHz, respectively. At these resonant frequencies, the magnitude of S_{11} is -15.72 dB , -33.33 dB , and -17.25 dB , and the magnitude of S_{21} is -1.51 dB , -0.14 dB , and -1.25 dB , respectively.

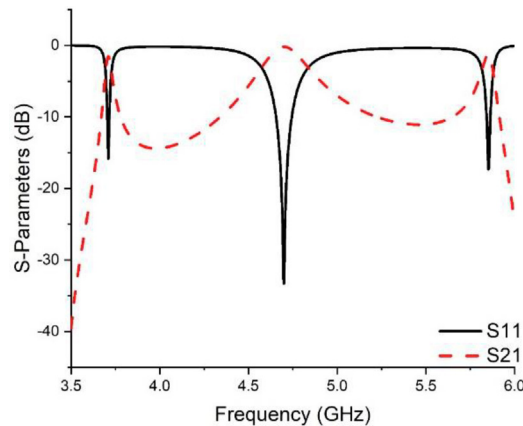


Fig. 3. Frequency vs. S11 and S21.

5. Different design layouts for the proposed structure

Five layout structures of unit cells were designed, and their S-parameters were extracted and analyzed shown in Fig. 4. For example, in design 1 only one split ring resonator is used and has a split gap and thickness of 1 mm. Design 1 shows the S11 and S21 at one resonant frequency of 4.6 GHz with -29.6 dB and -0.28 dB, respectively. Design 2 consists of two split ring resonators placed at -45° with each other. The second ring resonator's thickness and the split gap are 0.8 mm. Therefore, design 2 operates at resonance frequencies of 3.8 and 4.6 GHz. The S11 values at these frequencies are -15.5 dB and 29.9 dB, whereas the S21 values are -1.5 dB and -0.2 dB. Design 3 consists of three split ring resonators placed at -45° to each other. The third resonator has a thickness and split gap of 0.6 mm. Design 3 operates at three frequencies which are 3.62 GHz, 4.69 GHz, and 5.73 GHz. The S11 values are -13.1 dB, -30.0 dB, and -16.1 dB at these frequencies. The S21 values for the same frequencies are -2.1 dB, -0.2 dB, and -1.4 dB. Design 4 consists of four split ring resonators, placed -45° to each other. In this design, the split gap and thickness of the fourth ring resonator are kept at 0.4 mm. Design 4 operates at three different resonant frequencies 3.71 GHz, 4.71 GHz, and 5.75 GHz. The S11 values at these frequencies are -13.5 dB, -29.6 dB, and -15.1 dB, whereas S21 values are -2.1 dB, -0.2 dB, and -1.6 dB. Our final design structure consists of five split ring resonators, where the fifth layer split gap and thickness is 0.2 mm. Our final design operates at three resonant frequencies, i.e. 3.7275 GHz, 4.7075 GHz, and 5.9325 GHz, with higher S-parameters than all the previous four designed structures. The S11 values at these frequencies are -15.72 dB, -33.33 dB, and -17.25 dB, whereas S21 values are -1.51 dB, -0.14 dB, and -1.25 dB, respectively. For different design configurations, frequency is shown against S11 and S21 in Fig. 5.

6. Effect of different substrates on the unit cell performance

Three substrate materials were employed to find the optimal substrate for the proposed design to examine its performance. FR-4, Rogers RO 4350B, and Rogers RT 5880 are substrates. The physical properties of three different substrates, namely F.R – 4, Rogers RO 4350B, and RT 5880, have been reported. Specifically, the thickness, Dielectric Constant (D.K.), and Loss Tangent (L.T.) of the F.R – 4 substrate are 1.5 mm, 4.3, and 0.025, respectively. The Rogers RO 4350B substrate has a thickness of 1.524 mm, a Dielectric Constant (D.K.) of 3.66, and a Loss Tangent (L.T.) of 0.037. Lastly, the RT 5880 substrate has a thickness of 1.575 mm, a Dielectric Constant (D.K.) of 2.2, and a Loss Tangent (L.T.) of 0.009.

Therefore, the S-Parameters were separately analyzed for the above-given substrates. For example, with an FR-4 substrate, the unit cell operates at two different resonance frequencies, 3.59 GHz and 4.47 GHz. Therefore, the magnitude for S11 at these frequencies is -29.6 dB and -14.5 dB; for S21, the is -0.2 dB and -1.7 dB. With Rogers RO 4350B substrate, the unit cell operates at two resonance frequencies, 3.8 and 4.8 GHz. Therefore, the magnitude for S11 and S21 at these frequencies are -30.8 dB, -15.5 dB, and -0.2 dB, -1.5 dB, respectively. However, the proposed substrate material RT 5880 performs better regarding higher S-parameters magnitude than others. With RT 5880, the proposed design gives resonance at three frequencies, i.e. 3.7275 GHz, 4.7075 GHz, and 5.9325 GHz. Therefore, the magnitude of S11 at these three frequencies lies at -15.72 dB, -33.33 dB, and -17.25 dB. In the same way, the magnitude of S21 lies at -1.51 dB, -0.14 dB, and -1.25 dB.

$$f = \frac{1}{2\pi\sqrt{LC}} \quad (10)$$

$$C = \epsilon_0 \epsilon_r \frac{A}{D}(\mathbf{F}) \quad (11)$$

From equation (10), we can see that C is inversely proportional to resonance frequency (f), and from equation (11), C is directly proportional to the permittivity [35]. Hence, different substrates have different permittivity values, so resonance frequency also differs. Therefore, the resonance frequency of the unit cell moves towards higher values with lower values of substrate permittivity and vice versa. Fig. 6 shows various substrate materials' frequency versus reflection and transmission coefficient.

7. Impact of various gap sizes on the functionality of the proposed design

Five split-ring resonators are proposed in the proposed design. Each resonator's split gap is modified, and S- parameters are examined independently for each modification. The modifications are as follows:

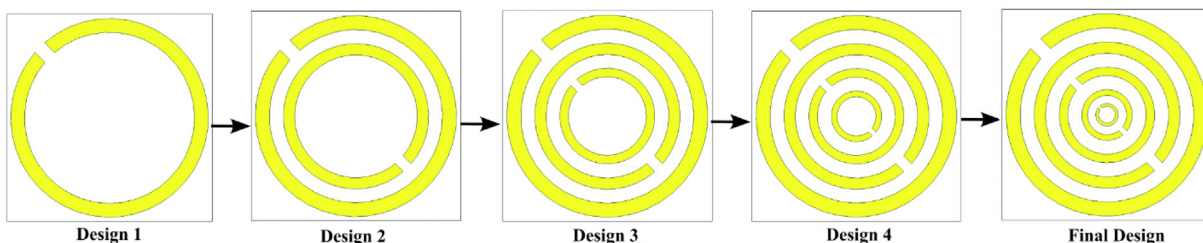


Fig. 4. Various structure designs for final design selection.

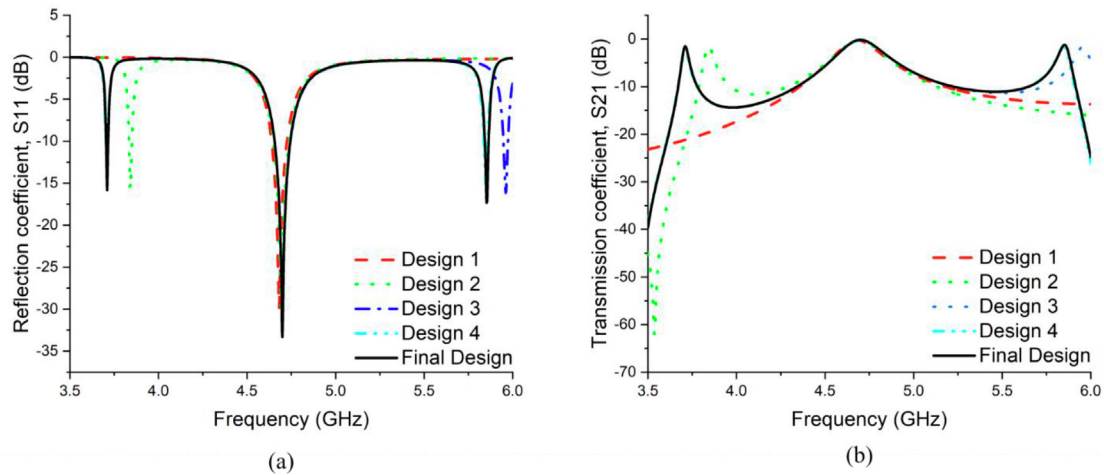


Fig. 5. Various design configurations (a) Frequency vs. S_{11} and (b) Frequency vs. S_{21} .

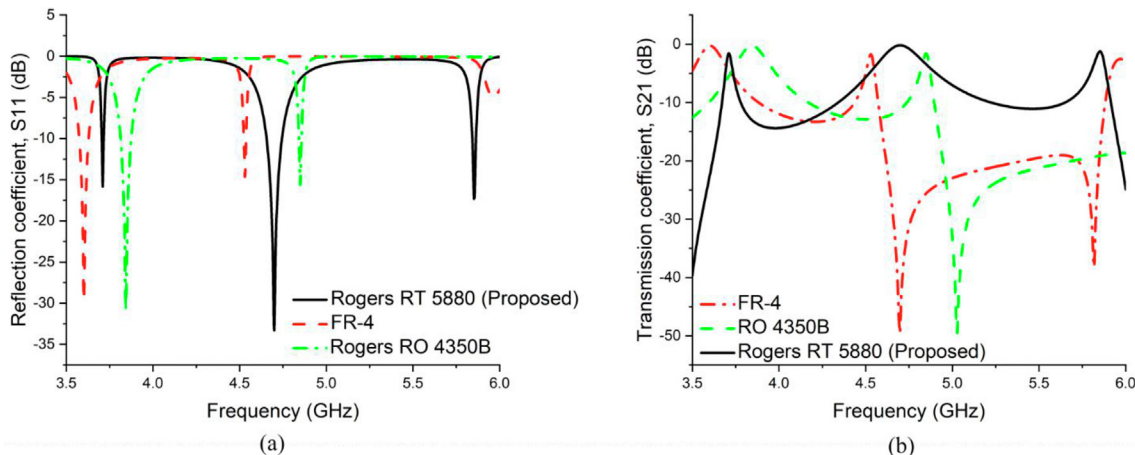


Fig. 6. Various substrate materials, (a) Frequency vs. S_{11} and (b) Frequency vs. S_{21} .

In **case 1**, the first ring has a split gap of 1.5 mm, followed by rings with split gaps of 1.3 mm, 1.1 mm, 0.9 mm, and 0.7 mm.

In **case 2**, the split gap of the first, second, third, fourth, and fifth rings is changed to 1.2 mm, 1 mm, 0.8 mm, 0.6 mm, and 0.4 mm, respectively. As shown in Fig. 7, the resonance frequency rises with an increasing split gap.

On the other end, as the final design **case 3**, the split gap of the first, second, third, fourth, and fifth is proposed to be 1 mm, 0.8 mm, 0.6 mm, 0.4 mm, and 0.2 mm, respectively. These gap sizes are suggested for better performance, as shown in Fig. 7.

8. The effect of various patch materials on the unit cell

Four different patch materials are used for the S-Parameters analysis of the proposed design. Using gold as a patch material on an RT 5880 substrate, the unit cell provides resonance at three frequencies, i.e., 3.71 GHz, 4.76 GHz, and 5.8 GHz. The magnitude for S_{11} at these frequencies is -14.9 dB, -32.4 dB, and -16 dB; for S_{21} , they are -1.7 dB, -1.2 dB, and -1.4 dB. Using Nickle as a patch material on the proposed substrate, the unit cell operates at only one resonance frequency, 4.5 GHz. As a result, the magnitude of S_{11} and S_{21} are -7.9 dB and -4.7 dB, respectively. Finally, using platinum and copper (proposed) as patch material separately, the unit cell operates almost at the same resonance frequency but less in magnitude. Because copper outperforms gold,

nickel, and platinum in terms of performance, it is eventually chosen as our final substrate material. Frequency vs S_{11} and S_{21} for various conducting materials is shown in Fig. 8.

9. Analysis of the proposed unit cell's surface current, E- and H-fields distributions

The proposed unit cell's field distribution analysis uses default 2×2 floquet mode. Fig. 11 shows the proposed unit cell's surface current at the three resonance frequencies, 3.7275 GHz, 4.7075 GHz, and 5.9325 GHz. The current flows through each metal ring for the first resonance frequency, and the strength of the current flow is high and uniform throughout all the metal rings, indicated by red colours. The current flow intensity is more significant for the outer two metal rings than the inner three at the second resonance frequency. Finally, the current flow intensity in the four inner metal rings is much higher for the third resonance frequency than the outer metal ring. On the other hand, The following equations can be used to define the E-field and H-field [36].

$$\nabla \times H = j + \frac{\partial D}{\partial t} \quad (12)$$

$$\nabla \times E = -\frac{\partial B}{\partial t} \text{ where } \nabla = \left[\frac{\partial}{\partial x}, \frac{\partial}{\partial y}, \frac{\partial}{\partial z} \right] \quad (13)$$

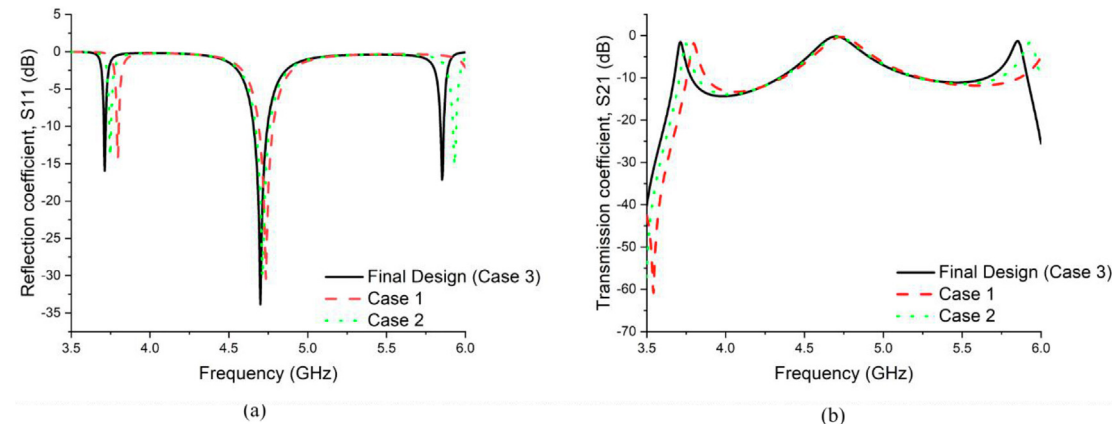
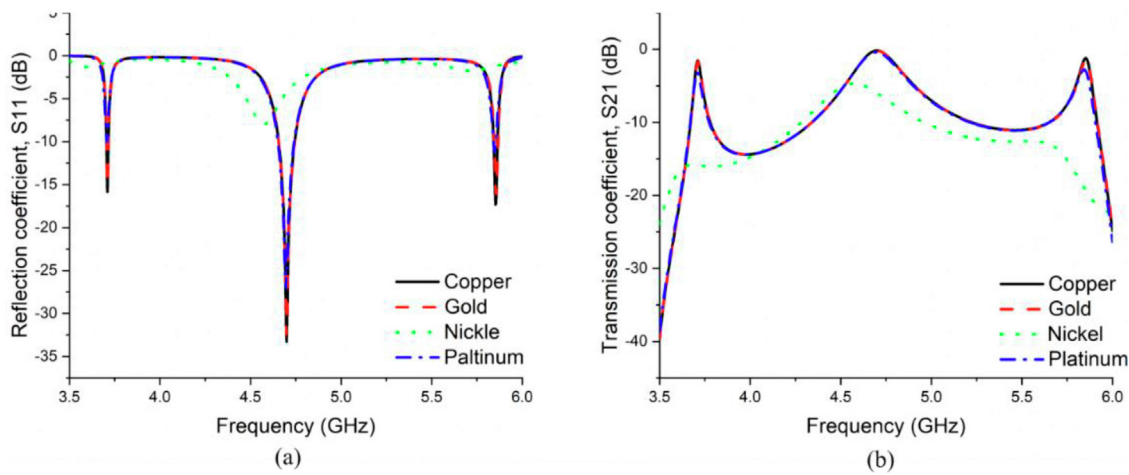
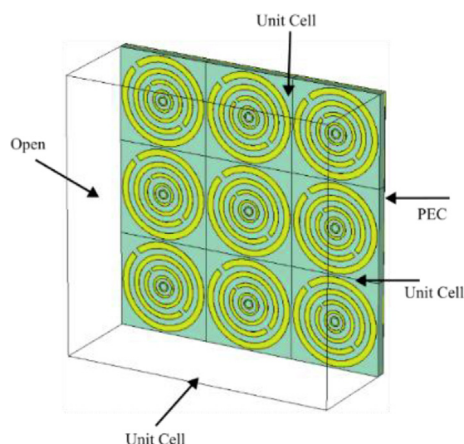
Fig. 7. Various split gap sizes (a) Frequency vs. S₁₁ and (b) Frequency vs. S₂₁.Fig. 8. Various conducting materials (a) Frequency vs. S₁₁ and (b) Frequency vs. S₂₁.

Fig. 9. The 3 × 3 array simulated arrangement.

The following two equations can express the electromagnetic field's materials interaction [37].

$$\mathbf{D}(\mathbf{t}) = \epsilon(\mathbf{t}) \times \mathbf{E}(\mathbf{t}) \quad (14)$$

$$\mathbf{B}(\mathbf{t}) = \mu(\mathbf{t}) \times \mathbf{H}(\mathbf{t}) \quad (15)$$

Fig. 12 shows the E-field distribution at three resonant frequencies. These frequencies are 3.7275 GHz, 4.7075 GHz, and 5.9325 GHz. The E-field distribution is present in almost each metal ring for the first resonance frequency, i.e., 3.7275 GHz. For the second resonance frequency, i.e., 4.7075 GHz, the E-field distribution appears in nearly three metal rings, whereas the intensity is less in the inner two metal rings. The E-field distribution is much higher in the middle metal ring than the other metal rings in the third resonance frequency, i.e., 5.9325 GHz. This is because every single ring of the proposed design has a strip gap, which acts like a capacitor. Therefore, the strength of the E-field is higher in these points. But on the other hand, the H-field around the wire at the receiver follow the equation (16) [38].

$$B = \frac{\mu I}{2\pi r} \quad (16)$$

Where μ is the free space permeability. **Fig. 13** depicts the H-field distribution at three distinct resonance frequencies, 3.7275 GHz, 4.7075 GHz, and 5.9325 GHz.

Nearly opposite excitations are seen in the H-field and E-field at all resonance frequencies. For a resonance frequency of 3.7275 GHz, the H-field distribution is present equally in all the metal rings, shown in red. At 4.7075 GHz, the H-field distribution is higher in the outermost metal ring than in all other metal rings. For 5.9325 GHz, the H-field allocation is increased in four metal rings compared to the outer metal ring.

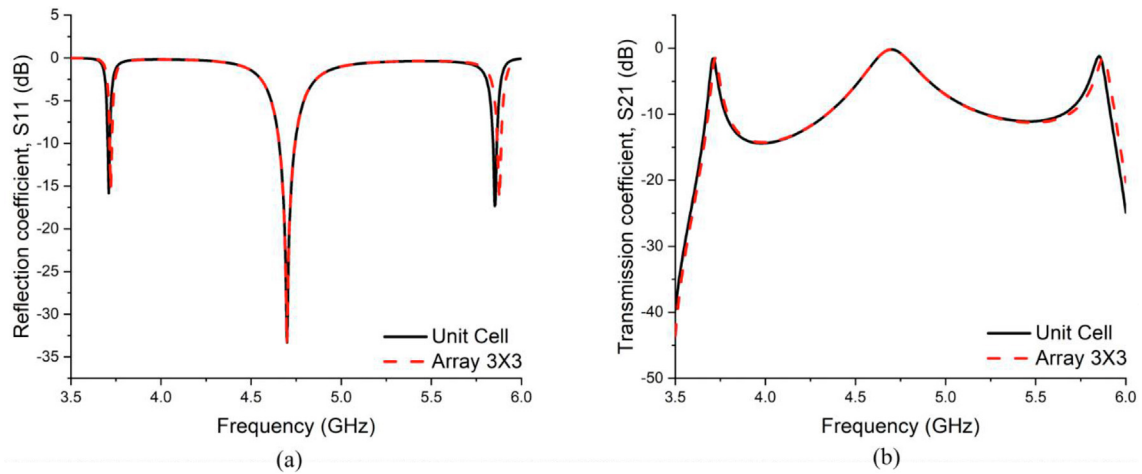


Fig. 10. Simulated results of Unit cell and Array 3×3 (a) Frequency vs. reflection coefficient (b) Frequency vs. transmission coefficient.

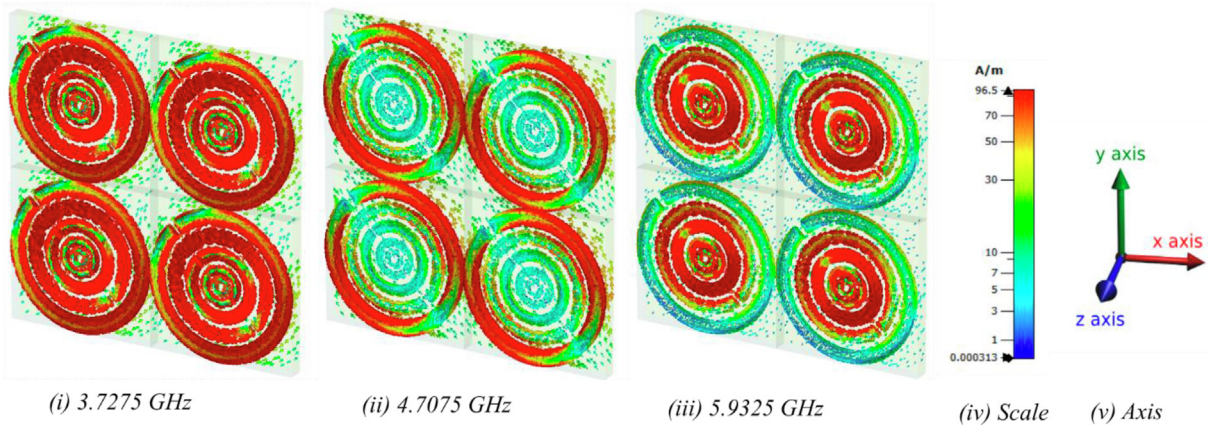


Fig. 11. Distribution of the Surface- current.

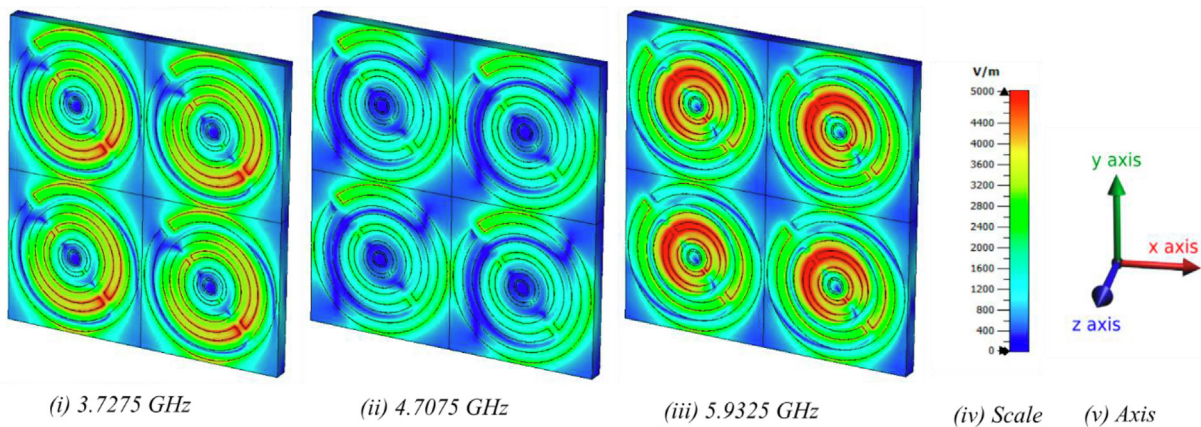


Fig. 12. Distribution of the E-field.

10. Results and discussion

The proposed unit cell's measured, and simulated S-Parameters are shown in Fig. 16. The proposed structure gives resonance at three frequencies, i.e., 3.7275 GHz, 4.7075 GHz, and 5.9325 GHz. The S11 magnitudes at these frequencies are -15.72 dB, -33.33 dB, and 17.25 dB, whereas the magnitudes for S21 are

-1.51 dB, -0.14 and -1.25 dB, respectively. Moreover, the effective medium parameters are calculated using the N.R.W. method mentioned in the equation (above). These parameters are relative permittivity (ϵ), relative permeability (μ), and refractive index (n). The real and imaginary parts of these parameters are shown in Fig. 14 (a), (b), and (c). Therefore, the proposed design can be categorized as a Double Negative Material (D.N.G.), as both the (ϵ) and (μ) are negative. The negative values of (ϵ) lie in the fre-

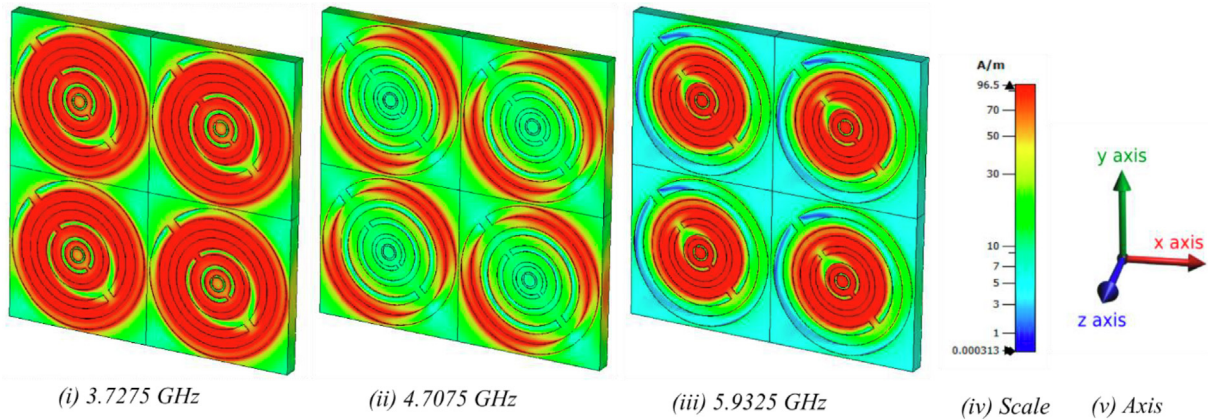


Fig. 13. Distribution of the H-field.

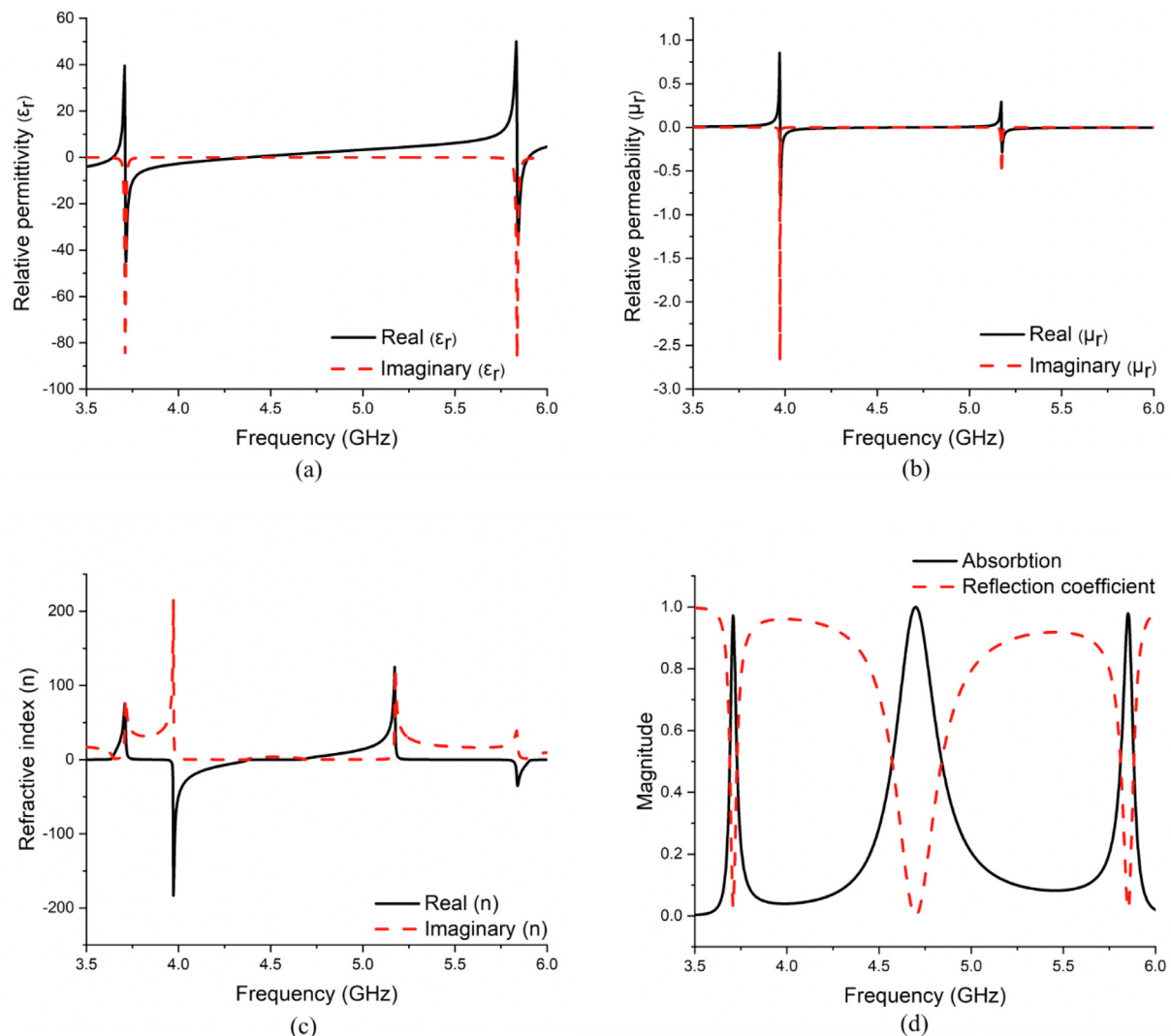


Fig. 14. (a) Frequency vs Relative permittivity, (b) Frequency vs. Relative permeability, (c) Frequency vs. Refractive index and (d) Frequency vs. Magnitude of absorption & reflection coefficient.

quency range of 3.7 GHz to 4.3 GHz and 5.8 GHz to 5.9 GHz. On the other hand, the negative values of the (μ) lie in the frequency range of 3.9 GHz to 4.2 GHz and 5.1 GHz to 5.3 GHz, respectively. Finally, the proposed structure was evaluated regarding its capability to absorb electromagnetic energy.

The following equation may be used to compute absorbance [8,31].

$$A(\omega) = 1 - R(\omega) - T(\omega) \quad (17)$$

Where $R(\omega) = |S11|^2$ and $T(\omega) = |S21|^2$ respectively. The magnitude of the absorption and reflection coefficient is shown in Fig. 14 (d). As we can see from the Fig. 14 (d), the absorption is near unity at all resonance frequencies, i.e., 3.7275 GHz, 4.7075 GHz, and 5.9325 GHz. Therefore, the absorption values at these frequencies are 97%, 99%, and 98%, respectively. Likewise, the percentage of the reflection at the resonance frequencies are 0.125%, 0.056%, and 0.146%, respectively. The high energy rates can thus be captured using the proposed unit cell. It can simultaneously power wireless sensor nodes, batteries, and other electrical devices [5–8].

The proposed unit cell's S-Parameters are measured using a Vector Network Analyzer (VNA) has a model no of N5227A. Before working on the VNA, it was calibrated with an Agilent N4694-60001 calibration kit. Then, a particular waveguide in the frequency range (3–6 GHz) was chosen. Finally, two coaxial cables—

one for the transmitter and the second for the receiver—were used to link the VNA to the waveguides. Three different waveguide models were used to measure the S-Parameters. These models are the 340WCAS, 187WCAS, and 112WCAS, and they operate at frequencies ranging from 2.20 to 3.30 GHz, 3.95 to 5.85 GHz, and 7.05 to 10 GHz, respectively. The proposed unit cell is placed between these waveguides separately, one by one, to measure the S-Parameters. Fig. 15 (a), (b), and (c) shows the measurement setup, unit cell and array fabricated prototypes. The calculated results for S11 and S21 from VNA were saved in prn format. Finally, the prn data were imported into Excel and origin to plot the graphs. Fig. 16 (a) and (b) show the simulated and measured results for S11 and S21. As shown in Fig. 16, there is a slight variation in the simulated and measured data.

11. Array analysis of the unit cell

Generally, an array of the unit cell is required to demonstrate the acceptable exotic electromagnetic properties. Therefore, a 3X3 array structure is designed and analyzed, as shown in Fig. 9. The 3×3 array and the unit cell have a resonant point at the same frequencies. Fig. 10 (a) and (b) show the reflection coefficient (S11) and transmission coefficient (S21) in dB for both the unit and 3×3 array cell.

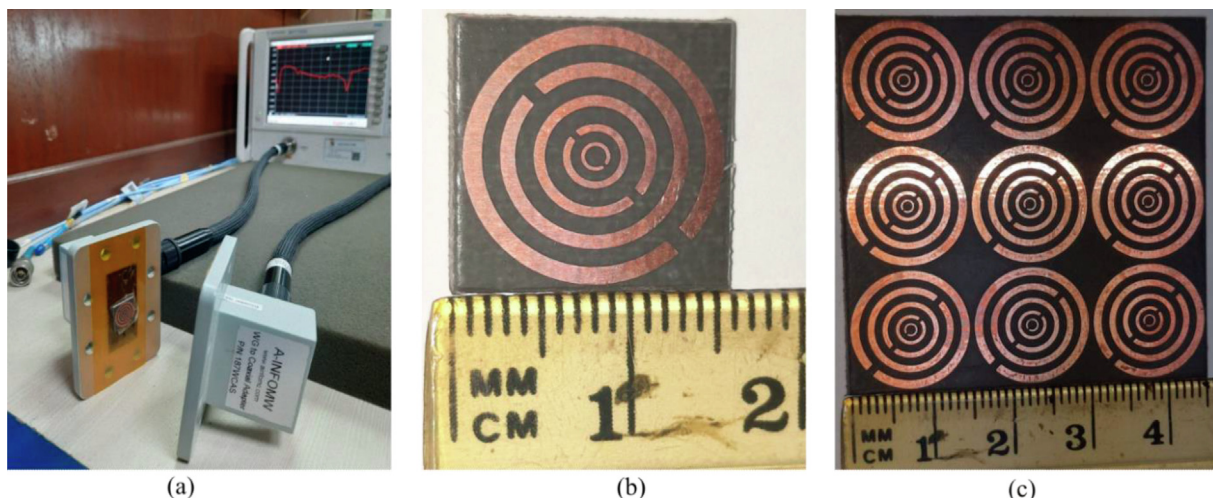


Fig. 15. Measurement setup (b) Fabricated unit cell prototype of $15 \times 15 \text{ mm}^2$ size (c) Fabricated Array 3×3 prototype of $45 \times 45 \text{ mm}^2$ size.

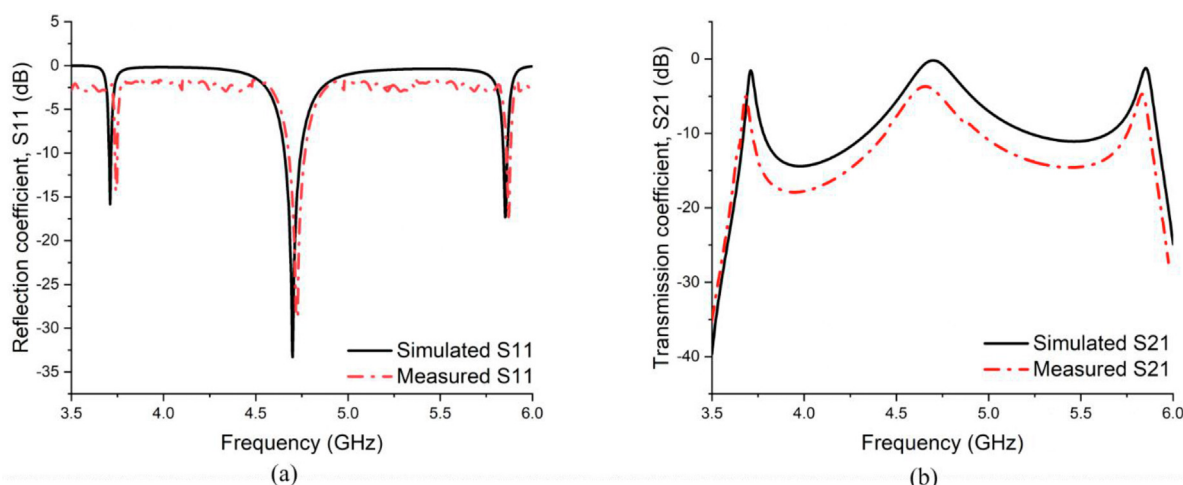


Fig. 16. Simulated and measured results (a) Frequency versus reflection coefficient (b) Frequency versus transmission coefficient.

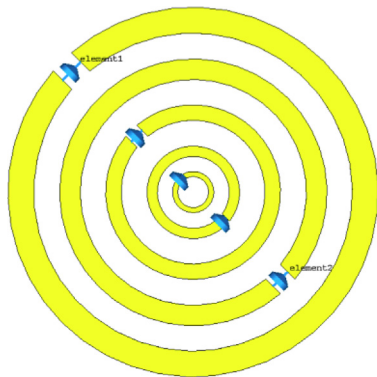


Fig. 17. Proposed unit cell absorber with the resistive loading for energy harvesting application.

The measured data can vary slightly for different reasons, i.e., VNA's calibration inaccuracy, coupling effects of Waveguides, dielectric substrate permittivity, and little change that can occur during Rogers RT 5880 substrate production.

11.1. Electromagnetic energy harvesting system based on the proposed design

Different experimental techniques were used to analyze the absorption of the proposed design. Fig. 18 (a) depicts the impact

of polarization angle change (ϕ) on absorption response under normal incidence. Similar absorption responses are recorded at 3.7275 and 4.7075 GHz; however, the absorption response at 5.9325 GHz shifts somewhat higher as ϕ rises. The absorption response for different oblique incidence angles (θ) with constant $\phi = 0^\circ$, under TE polarization and TM polarization is shown in Fig. 18 (b) and (c). Fig. 18 (b) shows how the oblique angle changes using TE polarization. Here, the electric field direction is kept constant while the magnetic field and wave propagation vector is rotated by an angle (θ).

In contrast, maintaining the magnetic field direction constant while varying the electric field and wave propagation vector by angle (θ) yields the TM polarization map shown in Fig. 18 (c). As a result, it is determined that the suggested triple-layer flexible design is a wide-angle absorber with an 89% absorption level up to 45° angle for TE polarization and a 91% absorption level up to 45° angle for TM polarization. Fig. 17 shows various load resistances positioned between the gaps of each ring resonator to investigate the wave absorption and associated electromagnetic energy harvesting performance. Fig. 18 (d) illustrates that the load resistance levels cause the absorption frequency shift expected in the final rectenna system after integrating the RF-DC rectification electronic circuit with the D.C. load to the design. As a result, it is vital to examine the resistive loading of unit cell systems in R.F. energy harvesting applications.

The harvesting efficiency (%) of metamaterial harvester (η) is defined by [39],

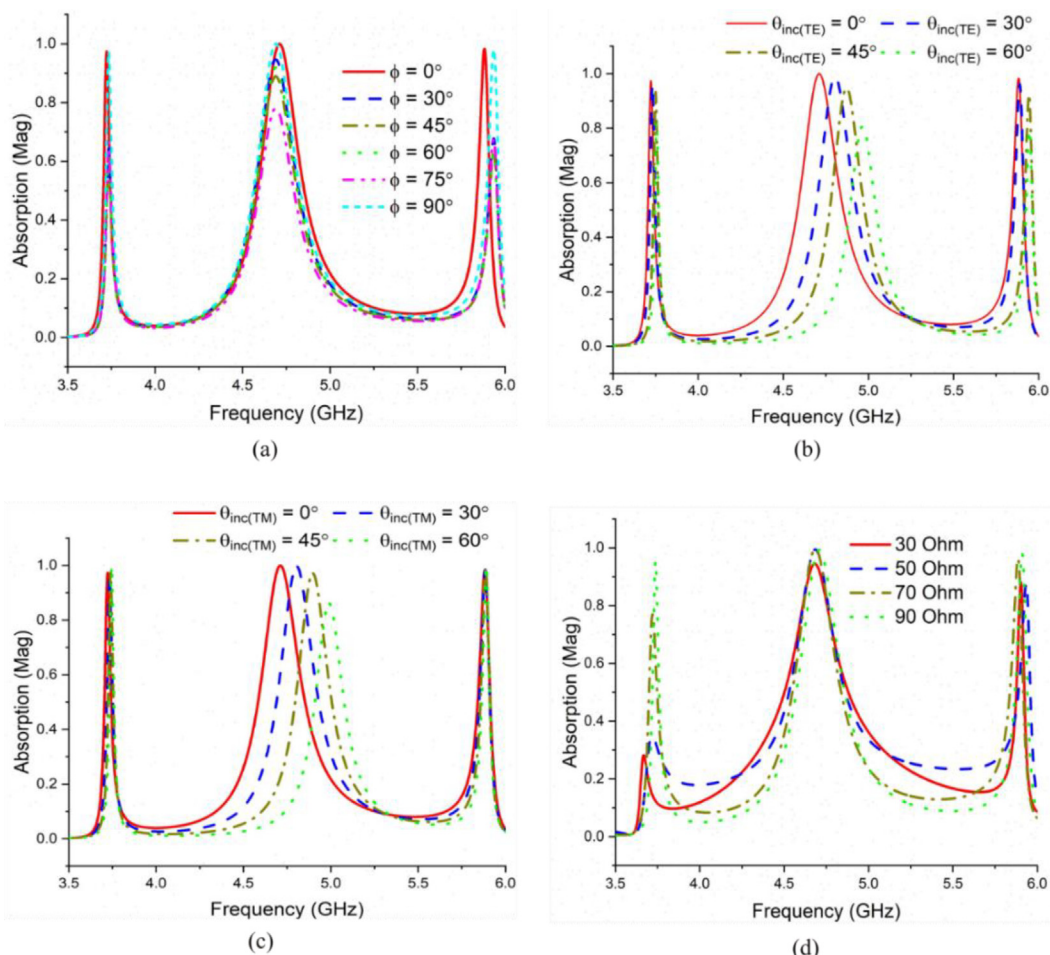


Fig. 18. Frequency vs. absorption (a) Various polarization angle (b) TE polarization with varying θ_{inc} angle (c) TM polarization with varying θ_{inc} angle (d) Absorption response depending on load resistance.

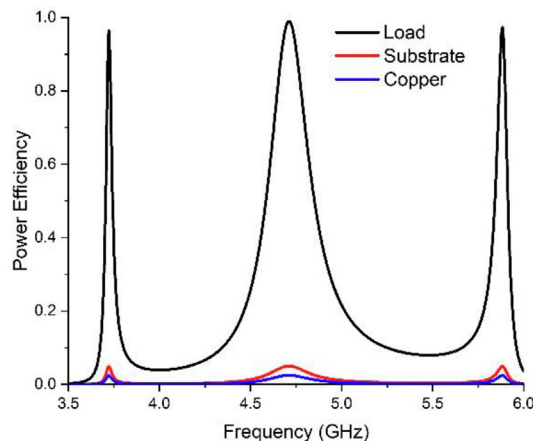


Fig. 19. Power distribution within the unicell after it experiences full absorption.

$$\eta = \frac{P_{load}}{P_{incident}} \times 100 \quad (18)$$

The variables P_{load} and $P_{incident}$ refer to the overall time-averaged power that is dissipated in the resistors and transmitted to the metamaterial harvester, respectively. In order to comprehend the distribution of dissipated power within the unit cell, the power loss in the resonator, the dielectric substrate, and the resistive load were calculated using full-wave simulation at a range of frequencies. 98% of the absorbed power was dissipated across the load, while approximately 3% was dissipated in both the substrate and the copper traces, as shown in Fig. 19. The power distribution within the unit cell differs significantly from previously examined metamaterial absorbers, where most designs relied on the loss in the dielectric substrates as the primary contributor to power dissipation.

The proposed metamaterial unit cell structure is compared to existing unit cell structures in Table 2. According to the study, the proposed unit cell.

structure covers the tri-band frequencies with double negative metamaterial properties. As a result, the overall performance of the proposed unit cell outperforms that of the structure mentioned in Table 2.

12. Conclusion

In conclusion, a new metamaterial unit cell has been proposed, which consists of five split-ring resonators arranged concentrically and capable of collecting electromagnetic energy. The study successfully demonstrated the numerical and experimental validation of the structure's capacity to absorb electromagnetic energy at frequencies of 3.7275 GHz, 4.7075 GHz, and 5.9325 GHz. The frequencies above encompass the S and C bands. The proposed design demonstrates a notable absorption level within the three designated bands. The absorption efficiencies corresponding to these spectral bands are 97%, 99%, and 98%, respectively. The wave absorption and electromagnetic energy harvesting capability were tested by placing different load resistances between the gaps of each ring resonator. The findings indicate that the triple-layer flexible design proposed in this study functions as a wide-angle absorber, exhibiting absorption levels of 89% for T.E polarisation and 91% for T.M polarisation up to a 45° angle. The proposed metamaterial absorber's high absorption coefficient, compact size, and thinness provide substantial benefits over traditional electromagnetic energy harvesting systems. Therefore, the proposed structure is an excellent choice for energy

Table 2
The performance of previous electromagnetic energy harvesters in the literature is compared with the proposed metamaterial energy harvester.

Parameters	Ref. [40]	Ref. [41]	Ref. [42]	Ref. [43]	Ref. [44]	Ref. [45]	Proposed Unit Cell
Number of Absorption Bands	Single	Single	Dual	Triple	Dual	Dual	Triple
Absorption Frequency (GHz)	3	2.4	3.368, 7.5	1.75, 2.17, 2.6	24, 42	24, 42	3.7275, 4.7075, 5.9325
Absorption Efficiency (%)	100	99.9	100, 95.97	96.91, 96.41, 90.12	98.2, 99.7	98.2, 99.7	97.99, 98
Dimension at lowest Absorption Frequency	$0.07\lambda_0 \times 0.07\lambda_0 \times 0.026\lambda_0$	$0.84\lambda_0 \times 0.84\lambda_0 \times 0.013\lambda_0$	$0.22\lambda_0 \times 0.2\lambda_0 \times 0.0058\lambda_0$	$0.2\lambda_0 \times 0.2\lambda_0 \times 0.036\lambda_0$	$0.011\lambda_0 \times 0.011\lambda_0 \times 0.0012\lambda_0$	$0.011\lambda_0 \times 0.011\lambda_0 \times 0.0012\lambda_0$	$0.18\lambda_0 \times 0.18\lambda_0 \times 0.019\lambda_0$
Wide incident angle insensitivity	No	No	No	No	Yes	Yes	Yes

harvesting applications because it collects and stores electromagnetic energy efficiently.

Declaration of Competing Interest

The authors declare that they have no known competing financial interests or personal relationships that could have appeared to influence the work reported in this paper.

Acknowledgements

This work is supported by the Faculty of Engineering, Multimedia University, Cyberjaya, Malaysia, under research grant RDTC/221039, TM R&D.

References

- [1] E. Reyes-Vera, D.E. Senior, J.M. Luna-Rivera, F.E. López-Giraldo, Advances in electromagnetic applications and communications, *TecnoLógicas* 21 (43) (2018) 9–13, <https://doi.org/10.22430/22565337.1052>.
- [2] J. Botero Valencia, L. Castaño Londoño, and D. Marquez Viloria, "Trends in the Internet of Things," *TecnoLógicas*, vol. 22, no. 44, pp. I-II, 2019, doi: 10.22430/22565337.1241.
- [3] D. Liu, W. Hong, T.S. Rappaport, C. Luxey, W. Hong, What will 5G Antennas and Propagation Be?, *IEEE Trans Antennas Propag.* 65 (12) (2017) 6205–6212, <https://doi.org/10.1109/TAP.2017.2774707>.
- [4] S. M. A. Huda, M. Y. Arafat, and S. Moh, "Wireless Power Transfer in Wirelessly Powered Sensor Networks : A Review of Recent Progress," 2022.
- [5] A.A.G. Amer, S.Z. Sapuan, N. Nasimuddin, A. Alphones, N.B. Zinal, A comprehensive review of metasurface structures suitable for RF energy harvesting, *IEEE Access* 8 (2020) 76433–76452, <https://doi.org/10.1109/ACCESS.2020.2989516>.
- [6] J. Enayati, P. Asef, Review and Analysis of Magnetic Energy Harvesters : A Case Study for Vehicular Applications, *IEEE Access* 10 (August) (2022) 79444–79457, <https://doi.org/10.1109/ACCESS.2022.3195052>.
- [7] Y. Zhang, J. Zhao, J. Cao, and B. Mao, "Microwave metamaterial absorber for non-destructive sensing applications of grain," *Sensors (Switzerland)*, vol. 18, no. 6, 2018, doi: 10.3390/s18061912.
- [8] Y.Z. Cheng, C. Fang, Z. Zhang, B. Wang, J. Chen, R.Z. Gong, A compact and polarization-insensitive perfect metamaterial absorber for electromagnetic energy harvesting application, 2016 Prog. Electromagn. Res. Symp. PIERS 2016 - Proc. 1 (2016) 1910–1914, <https://doi.org/10.1109/PIERS.2016.7734828>.
- [9] A. Mavaddat, S.H.M. Armani, A.R. Erfanian, Millimeter-wave energy harvesting using 4×4 microstrip patch antenna array, *IEEE Antennas Wirel. Propag. Lett.* 14 (2015) 515–518, <https://doi.org/10.1109/LAWP.2014.2370103>.
- [10] P. Chomtong, K. Rakdaniklang, P. Krachodnok, K. Bandudej, P. Akkaraekthalin, A Dual-Band Metasurface Reflector Using Ring Resonator with Interdigital Capacitor, *IEEE Access* 9 (2021) 62074–62083, <https://doi.org/10.1109/ACCESS.2021.3073870>.
- [11] S. Science, N. Series, and G. Crater, "Metamaterials and Negative Refractive Index Author (s): D. R. Smith , J. B. Pendry and M . C . K . Wiltshire," vol. 305, no. 5685, pp. 788–792, 2015.
- [12] D. Catano-Ochoa, D. E. Senior, F. Lopez, and E. Reyes-Vera, "Performance analysis of a microstrip patch antenna loaded with an array of metamaterial resonators," 2016 IEEE Antennas Propag. Soc. Int. Symp. APSURSI 2016 - Proc., pp. 281–282, 2016, doi: 10.1109/APS.2016.7695849.
- [13] M.S. Rao, P.I. Basarkod, A novel complementary slotted split ring resonator loaded truncated arc patch antenna with enhanced performance, *Prog. Electromagn. Res. C* 101 (May) (2020) 203–218, <https://doi.org/10.2528/PIERC20031003>.
- [14] G. Acevedo-Osorio, E. Reyes-Vera, H. Lobato-Morales, Dual-Band Microstrip Resonant Sensor for Dielectric Measurement of Liquid Materials, *IEEE Sens. J.* 20 (22) (2020) 13371–13378, <https://doi.org/10.1109/JSEN.2020.3005185>.
- [15] M. Gil, J. Bonache, F. Martín, Metamaterial filters: A review, *Metamaterials* 2 (4) (2008) 186–197, <https://doi.org/10.1016/j.metmat.2008.07.006>.
- [16] J.D. Baena, J. Bonache, F. Martin, R.M. Sillero, F. Falcone, T. Lopetegi, M.A.G. Laso, J. Garcia-Garcia, I. Gil, M.F. Portillo, M. Sorolla, Equivalent-circuit models for split-ring resonators and complementary split-ring resonators coupled to planar transmission lines, *IEEE Trans. Microw. Theory Tech.* 53 (4) (2005) 1451–1461.
- [17] U.S. Pranav, S. Sudheesh, P. Stanly, S. Sankar, R. Devika, A. Pradeep, Metamaterial Based Energy Harvester, *Procedia Comput. Sci.* 93 (September) (2016) 74–80, <https://doi.org/10.1016/j.procs.2016.07.184>.
- [18] A. Benayad, M. Tellache, A compact energy harvesting multiband rectenna based on metamaterial complementary split ring resonator antenna and modified hybrid junction ring rectifier, *Int. J. RF Microw. Comput. Eng.* 30 (2) (2020) 1–11, <https://doi.org/10.1002/mmce.22031>.
- [19] A.F. Almutairi, M.S. Islam, M. Samsuzzaman, M.T. Islam, N. Misran, M.T. Islam, A complementary split ring resonator based metamaterial with effective medium ratio for C-band microwave applications, *Results Phys.* vol. 15, no. July (2019), <https://doi.org/10.1016/j.rinp.2019.102675> 102675.
- [20] V.S. Sankar, R. Kumari, B. Choudhury, "Metamaterial-Inspired Rectenna Loaded with a DR for RF Energy Harvesting", 2018 IEEE Indian Conf. Antennas Propagation, INCAP 2018 (2018) 14–16, <https://doi.org/10.1109/INCAP.2018.8770854>.
- [21] B. Alavikia, T. S. Almoneef, O. M. Ramahi, B. Alavikia, T. S. Almoneef, and O. M. Ramahi, "Electromagnetic energy harvesting using complementary split-ring resonators Electromagnetic energy harvesting using complementary split-ring resonators," vol. 163903, 2014, doi: 10.1063/1.4873587.
- [22] B. Alavikia, T. S. Almoneef, and O. M. Ramahi, "Complementary split ring resonator arrays for electromagnetic energy harvesting," *Appl. Phys. Lett.*, vol. 107, no. 3, pp. 1–6, 2015, doi: 10.1063/1.4927238.
- [23] B. Alavikia, T. S. Almoneef, and O. M. Ramahi, "Wideband resonator arrays for electromagnetic energy harvesting and wireless power transfer," *Appl. Phys. Lett.*, vol. 107, no. 24, 2015, doi: 10.1063/1.4937591.
- [24] R. Das, E. McGlynn, M. Yuan, H. Heidari, Serpentine-shaped metamaterial energy harvester for wearable and implantable medical systems, *Proc. - IEEE Int. Symp. Circuits Syst.* vol. 2021-May (2021), <https://doi.org/10.1109/ISCAS51556.2021.9401288>.
- [25] A. Hoque, M.T. Islam, Numerical Analysis of Single Negative Broadband Metamaterial Absorber Based on Tri Thin Layer Material in Visible Spectrum for Solar Cell Energy Harvesting, *Plasmonics* 15 (4) (2020) 1061–1069, <https://doi.org/10.1007/s11468-020-01132-8>.
- [26] K.S.L. Albadri, Journal of King Saud University – Science Electromagnetic broad band absorber based on metamaterial and lumped resistance, *J. King Saud Univ. - Sci.* 32 (1) (2020) 501–506, <https://doi.org/10.1016/j.jksus.2018.07.013>.
- [27] S. Bhattacharyya, S. Ghosh, and K. Vaibhav Srivastava, "Bandwidth-Enhanced Metamaterial Absorber Using Electric Field-Driven Lc resonator For Airborne Radar Applications," *Microw. Opt. Technol. Lett.*, vol. 55, no. 9, 2013, doi: 10.1002/mop.
- [28] M. Bağmanci, M. Karaaslan, O. Altintas, F. Karadağ, E. Tetik, M. Bakır, Wideband metamaterial absorber based on CRRs with lumped elements for microwave energy harvesting, *J. Microw. Power Electromagn. Energy* 52 (1) (2018) 45–59, <https://doi.org/10.1080/08327823.2017.1405471>.
- [29] K.P. Kaur, T. Upadhyaya, Wide-angle and polarisation-independent tri-band dual-layer microwave metamaterial absorber, *IET Microwaves, Antennas & Propagation* 12 (8) (2018) 1428–1434.
- [30] K. P. Kaur, T. Upadhyaya, and M. Paland, "Dual-Band Polarization-Insensitive Metamaterial Inspired Microwave Absorber for LTE-Band Applications," vol. 77, no. August, pp. 91–100, 2017.
- [31] K.P. Kaur, T. Upadhyaya, Performance evaluation of wide-angle ultrathin microwave metamaterial absorber with polarization independence, *Adv. Electromagn.* 7 (4) (2018) 71–77, <https://doi.org/10.7716/AEM.V714.761>.
- [32] "CST Studio Suite 3D EM simulation and analysis software." <https://www.3ds.com/products-services/simulia/products/cst-studio-suite/> (accessed Nov. 21, 2022).
- [33] E. Ahmed, M.R.I. Faruque, A.M. Tamim, M.T. Islam, M.F.B. Mansor, M.B. Ahmed, "Enhancement of magnetic field intensity with a left-handed metamaterial tunnel resonator for obstacle sensing", *Chinese. J. Phys.* 70 (2021) 91–105.
- [34] A.B. Numan, M.S. Sharawi, Extraction of material parameters for metamaterials using a full-wave simulator [education column], *IEEE Antennas Propag. Mag.* 55 (5) (2013) 202–211, <https://doi.org/10.1109/MAP.2013.6735515>.
- [35] M.R. Islam, M.T. Islam, M.S. Soliman, M.H. Baharuddin, K. Mat, A.M. Moubarik, S.H.A. Almalki, Metamaterial based on an inverse double V loaded complementary square split ring resonator for radar and Wi - Fi applications, *Sci. Rep.* 11 (1) (2021), <https://doi.org/10.1038/s41598-021-01275-6>.
- [36] MAREK S. WARTAK, "Introduction to Metamaterials," vol. 1, pp. 30–34, 2011.
- [37] M. M. Bait-suwalam, "Electromagnetic Field Interaction with Metamaterials," vol. c, no. 1, pp. 1–19.
- [38] "Lesson Explainer: The Magnetic Field due to a Current in a Straight Wire | Nagwa." <https://www.nagwa.com/en/explainers/909137183476/> (accessed Dec. 03, 2022).
- [39] E. Karakaya and F. Bagci, "Four-band electromagnetic energy harvesting with a dual-layer metamaterial structure," no. October, pp. 1–7, 2018, doi: 10.1002/mmce.21644.
- [40] T. S. Almoneef and O. M. Ramahi, "Metamaterial electromagnetic energy harvester with near unity efficiency," *Appl. Phys. Lett.*, vol. 106, no. 15, 2015, doi: 10.1063/1.4916232.
- [41] M. Bakır et al., "Electromagnetic energy harvesting by using tunable metamaterial absorbers," 2015 23rd Signal Process. Commun. Appl. Conf. SIU 2015 - Proc., pp. 467–470, 2015, doi: 10.1109/SIU.2015.7129860.
- [42] S. Khan, T.F. Eibert, A multi-resonant meta-absorber as an electromagnetic energy harvester, 2017 IEEE Antennas Propag. Soc. Int. Symp. Proc. vol. 2017-Janua (2017) 1091–1092, <https://doi.org/10.1109/APUSNCURSINRSM.2017.8072588>.
- [43] K.P. Kaur, T. Upadhyaya, M. Palandoken, C. Gocen, Ultrathin dual-layer triple-band flexible microwave metamaterial absorber for energy harvesting applications, *Int. J. RF Microw. Comput. Eng.* 29 (1) (2019) 1–7, <https://doi.org/10.1002/mmce.21646>.
- [44] F. Umaña-Idarraga, D. Cataño-Ochoa, S. Montoya-Villada, C. Valencia-Balvin, E. Reyes-Vera, Design of a perfect and multi-resonant metamaterial absorber for electromagnetic energy harvesting applications, *J. Phys.: Conf. Ser.* 2118 (1) (2021) 012005.